

FACILE SYNTHESIS OF MnO/CARBON/CARBON NANOTUBE NANOHYBRIDS USING DENTAL RESINS AS SOLVENT AND CARBON SOURCE

J. BAN^{a,b}, P. YANG^c, Y. XIAO^a, M. WANG^{a,d}, X. WANG^a, Y. XIAO^a, B. QIU^a, L. YANG^{a,b}, Z. LIU^a, C. ZHU^c, C. CHEN^b, Y.-J. CHENG^{a*}

^a Ningbo Institute of Materials Technology and Engineering, Chinese Academy of Science, 1219 Zhongguan West Rd, Ningbo, 315201, P.R. China

^b Nano Science and Technology Institute, University of Science and Technology of China, 166 Renai Rd, Suzhou, 215123, P.R. China

^c School of Chemistry and Chemical Engineering, Henan University of Technology, 100 Lianhua Street, Zhengzhou, 450000, P. R. China

^d Faculty of Materials Science and Chemical Engineering, Ningbo University, Ningbo, 315211, P. R. China

Manganese (II) Oxide (MnO) and its composites with carbon have attracted wide attention as high performance lithium-ion battery anode. An *in situ*, facile method for preparing MnO/carbon/carbon nanotubes nanohybrids has been developed using dental difunctional methacrylate monomers as solvent and carbon source. With this method, the solvent disposal process is totally circumvented. The MnO nanoparticles are homogeneously incorporated into the carbon matrix, within which the CNTs are homogeneously dispersed. Systematic characterization on the crystallographic phase and morphology of MnO, content and nature of carbon matrix, and electrochemical performance of the MnO/C/CNTs has been performed. A significant improvement of rate performance with the incorporation of CNTs has been observed compared to the bare MnO/C nanohybrids. It is confirmed by the significant reduction of the charge transfer impedance measured by electrochemical impedance spectroscopy.

(Received January 12, 2016; Accepted March 1, 2016)

Keywords: *in situ*; Pyrolysis; Lithium-Ion Battery; Manganese Oxide; Methacrylate; Carbon Nanotubes

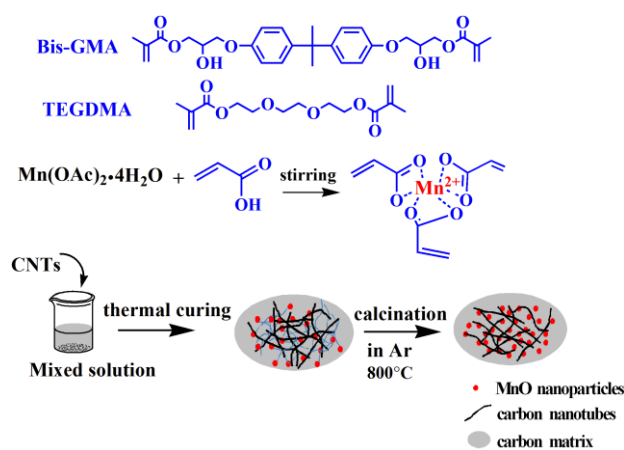
1. Introduction

Rechargeable lithium-ion batteries (LIBs) have become the dominant power source for consumer portable electronic devices. Owing to rapid technology development, there is an increasing demand for LIBs with better safety, higher energy density and longer cycle life [1, 2]. The commercial graphite anode suffers inferior capacity and operation safety risk [3, 4]. Various anode materials, such as transition metal oxides [5-9], silicon [1, 10-12], germanium [13-15], and tin oxides [16-18], have been studied as alternative anode in the last decade. Among these anode candidates, MnO is one of the most promising one because of its high theoretical capacity (756 mAh g⁻¹), low conversion potential (1.032 V vs Li⁺/Li) [19-21], good environmental benignity, natural abundance and low cost. However, the intrinsically poor electron conductivity, dramatic volume change during repeated lithiation/delithiation, and partial irreversibility of the lithiation/delithiation reaction result in deteriorated electrochemical performance [22, 23].

Synthesizing nanoscale MnO is an attractive strategy to tackle the above mentioned critical

*Corresponding author: chengyj@nimte.ac.cn

issues. Furthermore, compositing MnO with carbonaceous materials including hard carbon [19, 24], carbon nanotubes (CNTs) [25, 26] has been reported as another effective way to address the problem of MnO. Particularly, the excellent electronic conductivity and one-dimensional anisotropic structure feature of the CNTs hold great promise to improve the electrochemical kinetics of MnO.



Scheme 1. Schematic illustration of the process for preparing the MnO/C/Carbon Nanotubes nanohybrids.

Recently, a new strategy has been reported by our group to synthesize metal oxide/carbon nanohybrid LIB anodes, particularly TiO_2/C [27, 28]. Dental difunctional methacrylate monomers have been used as solvent and carbon source to control the morphology of TiO_2 . With this strategy, ultrasmall TiO_2 nanoparticles with the size in the range of around 5 nm (1 nm to 6 nm) are homogeneously embedded in the *in situ* formed carbon matrix. Peculiar electrochemical performance has been observed with the unique TiO_2/C nanohybrid anode. Based on our previous research work, here we extend our work to the synthesis of MnO/C nanohybrid anode. Furthermore, we would like to introduce CNTs into the nanohybrids to enhance electrochemical performance. Based on this concept, MnO/Carbon/CNT has been prepared successfully. Bisphenol A glycerolate methacrylate (Bis-GMA) and triethylene glycol dimethacrylate (TEGDMA) are used as carbon source and solvents as well (Scheme 1). Manganese acetate is dissolved in the resin mixture by forming coordination bonds between Mn^{2+} and COOH of the acrylic acid (AA). Furthermore, hydrophilic CNTs are dispersed in the resin solution by ultrasonication. The mixed solution is cured at moderate temperature with a thermal initiator of tert-Butyl Peroxy benzoate (TBPB). The thermosetting vinyl resins are *in situ* converted to carbon by pyrolysis at high temperature in argon; while MnO nanoparticles are simultaneously *in situ* synthesized within the carbon matrix. The MnO nanoparticles are uniformly embedded in the carbon matrix because the Manganese acetate is homogeneously incorporated in the cross-linked methacrylate network at molecular level. The addition of CNTs into the carbon matrix is supposed to enhance the electrochemical performance of the MnO/C nanohybrids. Finally, it is worth pointing out that a particular advantage associated with this strategy is that the tedious, costly, and environment unfriendly solvent disposal process can be totally circumvented.

2. Experimental

2.1 Materials and Synthesis Methods

All reagents were used as received without further purification. Manganese acetate tetrahydrate ($\text{Mn}(\text{CH}_3\text{COO})_2 \cdot 4\text{H}_2\text{O}$, $\geq 99\%$) and TBPB were purchased from Aladdin Industry Corporation. Acrylic acid was purchased from Sinopharm Group Co., Ltd. Bisphenol A glycerolate

methacrylate (Bis-GMA) and Triethylene glycol dimethacrylate (TEGDMA) were donated by Esstech, Inc., USA. Short carboxyl multiwall carbon nanotubes (>95 %, 0.5 μm - 2 μm length, 3.86 wt% of carboxyl group content) was purchased from Chengdu Organic Chemicals Co. Ltd., Chinese Academy of Sciences.

The detailed sample preparation process is as following (Scheme 1). 4.0 g $\text{Mn}(\text{CH}_3\text{COO})_2 \cdot 4\text{H}_2\text{O}$ was dissolved in 4.0 g acrylic acid with magnetic stirring and heating to around 40 $^\circ\text{C}$ for ten minutes. Then, various amounts of carbon nanotubes were dispersed into the mixed solution of Bis-GMA/TEGDMA resin (2:3 by mass ratio) by ultrasonication at 240 W for 2 h. Thereafter, 2 wt% of t-butyl Peroxy benzoate (TBPB) was added into the mixed solution and stirred for ten minutes. The final solution was transferred into a Polytetrafluoroethylene (PTFE) mould for polymerization. The thermal curing procedure was set at the sequence of 80 $^\circ\text{C}$ for 1 h, 110 $^\circ\text{C}$ for 2 h, and final 150 $^\circ\text{C}$ for 1 h. The polymerized nanohybrids were calcined at 800 $^\circ\text{C}$ under Argon atmosphere for 4 h with a ramp rate of 5 K/min starting from room temperature, followed by natural cooling to ambient condition. The calcined samples were finally ball milled for 150 min in total at a speed of 400 rpm and interval of 5 min for every 15 min ball milling.

2.2 Nanohybrids Characterization

The crystallographic phases of the MnO/C/CNTs nanohybrids were investigated by X-ray diffraction (XRD) (Bruker AXS D8 Advance, $\lambda=1.541 \text{ \AA}$, 2.2 kW) with 2θ ranged from 5 $^\circ$ to 90 $^\circ$.

The contents of MnO in the MnO/C/CNTs nanohybrids were determined by Thermo Gravimetric Analyzer (TGA, Mettler Toledo, Switzerland) with the temperature range set between 50 $^\circ\text{C}$ and 800 $^\circ\text{C}$ with a ramp rate of 20 K/min in air. The content of the CNTs is derived from the mass ratio between the CNTs and MnO in the original feeding materials source.

Field emission scanning electron microscope (FESEM) images were obtained with Hitachi S4800 scanning electron microscope (TOKYO, Japan) at an accelerating voltage of 4 kV. Gold sputtering was applied before imaging.

Transmission Electron Microscopy (TEM) experiment was conducted by putting a drop of aqueous sample suspension on copper grid. The measurement was carried out with a JEOL JEM-2100F TEM operated at 200 kV. The average sizes of the MnO nanoparticles were measured based on at least ten particles.

Raman data was collected on a Renishaw (in Via-reflex) at the wavelength of 532 nm.

The pore size distribution of the nanohybrids was obtained by the Barrett-Joyner-Halenda (BJH) method. Surface area was measured with the Brunauer-Emmett-Teller (BET) method. The vacuum point was set at 100 μm Hg. The desorption temperature range was set from 120 $^\circ\text{C}$ to 300 $^\circ\text{C}$ and held for 400 min at 300 $^\circ\text{C}$. The isothermal curve was collected by 60 data points.

2.3 Electrochemical Measurement

The working electrodes were fabricated by casting slurry onto a copper foil and dried at 90 $^\circ\text{C}$ in oven for 6 h. The slurry contained 80 wt% active material (MnO/C/CNTs nanohybrids), 10 wt% acetylene black (Super P), and 10 wt% Poly (vinylidene fluoride) (PVDF), which were dissolved in *N*-methyl-2-pyrrolidinone. After drying, the electrode sheet was pressed and punched into round disk electrode with the diameter of 13 mm and further dried at 80 $^\circ\text{C}$ for 6 h in oven. 2032 type half-cell was assembled using a pure lithium foil as counter electrode, Celgard 2300 as separator, and 1 M LiPF_6 in a mixture of ethylene carbonate (EC) and dimethyl carbonate (DMC) ($v/v = 1:1$) as the electrolyte. Cells were assembled in argon-filled glovebox with the concentrations of moisture and oxygen below 3.0 ppm. The galvanostatic cyclic charge/discharge measurements were carried out using a Land Battery Measurement System (Land, China) under current densities of 151 mA g^{-1} (0.2 C, 1 C = 756 mAhg^{-1}) in the voltage range of 3.00 V – 0.005 V vs. Li^+/Li at room temperature. The rate performance was measured with five cycles each at the current densities of 0.1 C, 0.2 C, 0.5 C, 1 C, 2 C, 5 C, 10 C, 20 C, and finally returned to 0.1 C. A PARSTAT 2273 potentiostat was employed for cyclic voltammetry measurement between 3 V and 0.01 V at a scanning rate of 0.1 mV s^{-1} . The electrochemical impedance spectrometry (EIS) was tested in a frequency range of from 1000 kHz to 10 MHz at room temperature.

3. Results & Discussions

The MnO contents in the MnO/C/CNTs nanohybrids were determined by TGA. As shown in Figure 1a, complete carbon loss occurs at around 600 °C. After 600 °C, the curves become flat, suggesting no further oxidation process happens. Nearly identical residual content of 63 % is confirmed by the TGA curves with different feeding mass of CNTs. It is well known that the high calcination temperature in air can lead to the modification of the Mn oxidation state. Mn_3O_4 is reported to be the most stable species in air due to the spinel-type structure[29]. Therefore, the final product after TGA is supposed to be $\text{Mn}^{2+}(\text{Mn}^{3+})_2\text{O}_4$. Theoretically, the oxidation of MnO to Mn_3O_4 causes 7.5 % mass gain [30]. Taking this factor into consideration, the MnO contents in the MnO/C/CNTs are calculated to be 58.6 %. According to the mass ratio between the CNTs and MnO in the original feeding materials source, the contents of CNTs in the nanohybrids are calculated to be 0 %, 2.5 %, 5.0 %, and 10.0 %, respectively. Even though the composition of CNTs is increasing, the total mass of the carbonaceous material of the nanohybrids are not modified significantly. It implies that CNTs influences the polymerization and consequent char forming process of the methacrylates. The increasing amount of CNTs increases the viscosity of the resin mixture. As a result, the gel point of the polymerized dimethacrylates reaches early, leading to relative less polymerization degree. Therefore, the char yield from the pyrolysis of the methacrylate is slightly decreased. Consequently, the total mass ratio of the carbonaceous materials (carbon from methacrylate and CNTs) is not changed significantly. For the reason of convenience, the samples are named after the mass percentage of CNTs in the following sections of the manuscript.

The XRD patterns of the MnO/C/CNTs nanohybrids are shown in Figure 1b. The diffraction peaks are located at 35.0 °, 40.8 °, 58.9 °, 70.3 ° and 74.1 ° respectively. All of the peaks can be well indexed to (1 1 1), (2 0 0), (2 2 0), (3 1 1) and (2 2 2) crystalline planes of pure cubic phase of MnO. The results indicate that the manganese acetate incorporated into the cross-linked methacrylate network can be fully converted to MnO during calcination in argon.

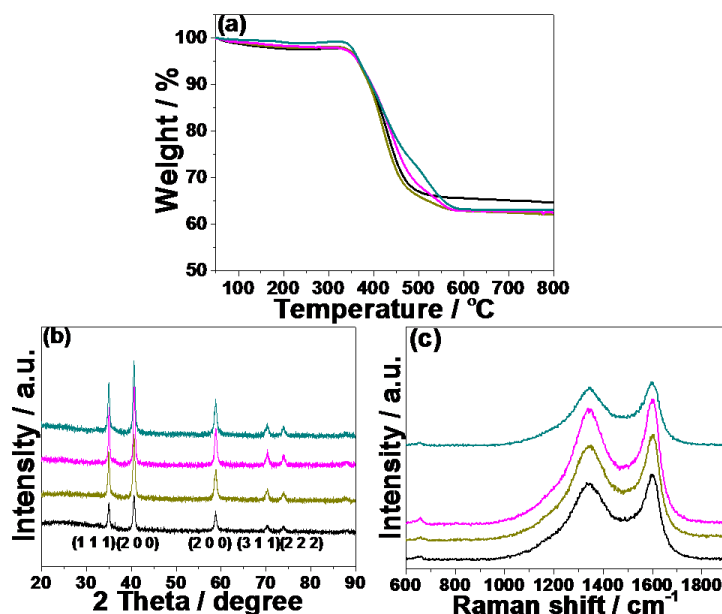


Fig. 1. TGA (a), XRD (b), and Raman (c) of the MnO/C/CNTs nanohybrids containing different mass contents of CNTs. (a) 0 %, black; (b) 2.5 %, dark yellow; (c) 5.0 %, magenta; (d) 10.0 %, dark cyan.

The Raman spectroscopy is exhibited in Figure 1c. The two peaks located at 1344 cm^{-1} and 1600 cm^{-1} are assigned to the D band and G band of carbon respectively. The 1344 cm^{-1} band

corresponds to the A_{1g} vibration mode of the disordered carbon (D-band) and the 1600 cm^{-1} band is related to the E_{2g} vibration mode of the ordered graphitic carbon (G-band)[30]. The integral intensity ratio of the G band over the D band (I_D/I_G) does not change significantly with respect to different samples (*ca.* 1.5). The results indicate that the variation of CNTs mass ratio does not influence nature of the overall carbonaceous matrix significantly. Furthermore, a typical Raman scattering peak of Mn_3O_4 located at 659 cm^{-1} is observed with all of the samples. The existence of Mn_3O_4 is likely due to the local heating effect and photo chemically induced transformation during the Raman measurements[31].

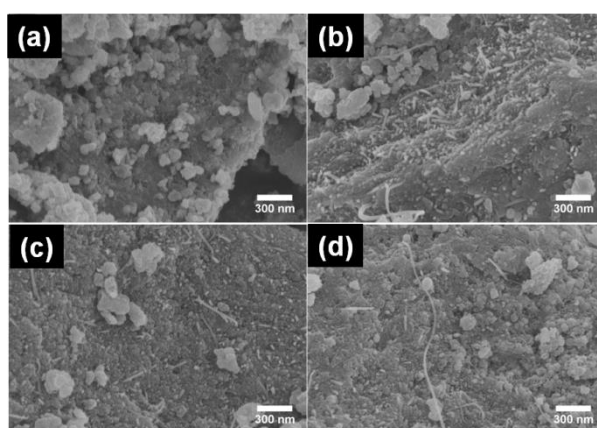


Figure 2. SEM images of MnO/C/CNTs nanohybrids with different mass contents of CNTs:

(a) 0 %, (b) 2.5 %, (c) 5.0 %, and (d) 10.0 %.

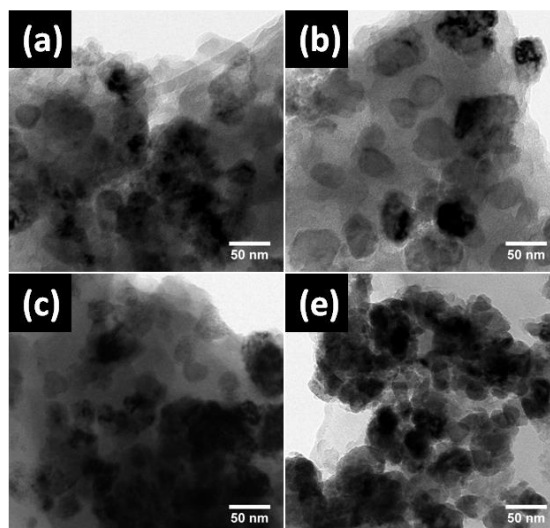


Figure 3. TEM images of MnO/C/CNTs nanohybrids with different mass contents of CNTs:

(a) 0 %, (b) 2.5 %, (c) 5.0 %, and (d) 10.0 %.

The morphology and microstructure of the MnO/C/CNTs nanohybrids are investigated by field emission scanning microscope (FESEM) and transmission electron microscopy (TEM). From Figure 2, it is observed that the CNTs are well embedded in the nanohybrids because only a short

part of CNTs extrudes from inside. The TEM images show that the MnO nanoparticles are well dispersed in the carbon matrix (Figure 3). From the high resolution TEM (HRTEM) images (Figure 4), it can be seen that crystalline MnO is coated with a carbon layer. The main lattice plane observed by HRTEM is (1 1 1) for all the MnO/C/CNTs nanohybrids. The N₂ adsorption/desorption curves are ascribed to typical IV type (Figure 5). Capillary coagulation leads to the occurrence of adsorption hysteresis, suggesting the pores are mainly mesoporous. Macrospores are also displayed in the pore size distribution curve. The Brunauer-Emmett-Teller (BET) specific surface areas are measured to be 48 m²/g, 104 m²/g, 70 m²/g, and 110 m²/g, respectively. The results reveal that the surface areas are enhanced significantly.

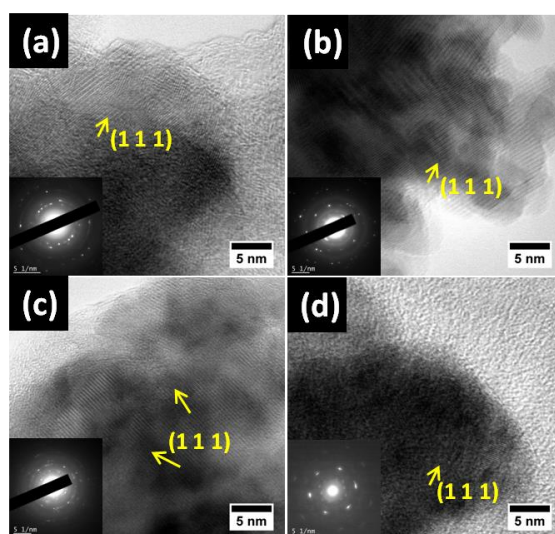


Fig. 4. HRTEM images of MnO/C/CNTs nanohybrids with different contents of CNTs: (a) 0 %, (b) 2.5 %, (c) 5.0 %, and (d) 10.0 %. Inserts: selected area electron diffraction (SAED) patterns.

The electrochemical performance of the MnO/C/CNTs nanohybrids has been explored. The voltage profiles of different cycles for the MnO/C/CNTs electrodes at the current density of 0.2 C (151 mA g⁻¹) are shown in Figure 6. Without CNTs, the discharge capacity of MnO/C decays seriously from the initial 833 mAh g⁻¹ to 211 mAh g⁻¹ after 100 cycles. Nevertheless, reversible capacity has been improved due to introduction of the CNTs. It is owing to the excellent electron conductivity of CNTs which facilitates the migration of electrons and relevant electrode reactions. The cycling performance of the MnO/C/CNTs electrodes at 0.2 C (151 mA g⁻¹) are shown in Figure 7. All electrodes exhibit stable cycling capabilities. After 100 cycles, the reversible specific capacities are 291 mAh g⁻¹, 260 mAh g⁻¹, and 296 mAh g⁻¹.

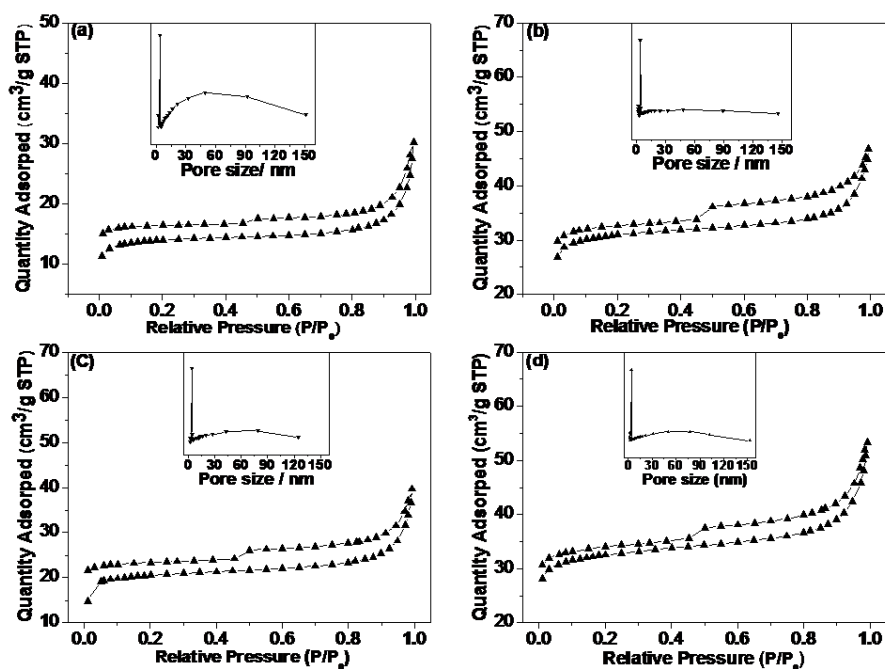


Fig 5. Nitrogen adsorption–desorption isotherm curves of MnO/C/CNTs with different CNTs contents: (a) 0 %, (b) 2.5 %, (c) 5.0 %, and (d) 10.0 %. Inserts are pore size distribution of MnO/C/CNTs nanohybrids.

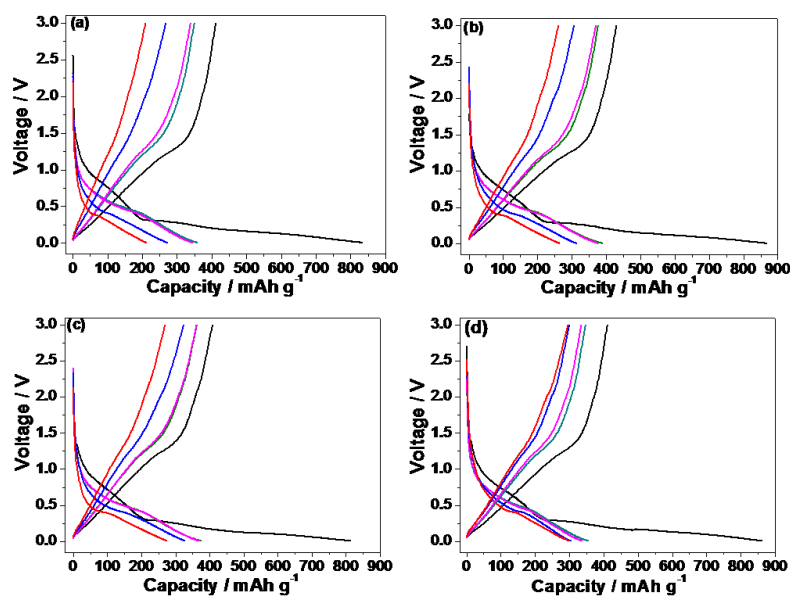


Fig. 6. Discharge and charge voltage profiles of MnO/C/CNTs nanohybrids with different contents of carbon nanotubes at 0.2 C (151 mA g^{-1}): (a) 0 %, (b) 2.5 %, (c) 5.0 %, and (d) 10.0 %. Profile of the 1st cycle, black; the 5th cycle, olive; the 10th cycle, magenta; the 50th, blue; and the 100th cycle, red.

Regarding rate performance, the electrodes are tested at different current densities from 0.1 C to 20 C ($1 \text{ C} = 756 \text{ mA g}^{-1}$) (Figure 8). It is observed that MnO/C/CNTs-2.5% displayed the best performance from 0.1 C to 5 C. Especially at 2 C (1512 mA g^{-1}), the capacity is as high as 153 mAh

g^{-1} , making a remarkable improvement compared with MnO/C (90 mAh g^{-1}). An obvious improvement is also achieved with the incorporation of CNTs at 5 C (3780 mA g^{-1}). Two major reasons are responsible for the electrochemical performance improvement. On one hand, enlarged specific surface area increases the contact between electrolyte and electrode. Consequently, it facilitates the transportation of lithium ions. On the other hand, the CNTs facilitate electron transfer within the composites by building additional interconnections between manganese oxides and carbon matrix as observed in the SEM images. At very high current density (10 C), the capacities of the nanohybrids with CNTs are still much better than the bare MnO/C sample (from 19 mAh g^{-1} to 25 mAh g^{-1} compared to 13 mAh g^{-1}). The results suggest that the CNTs play an important role in improving the rate performance compared to the bare MnO/C electrode even at very high current density. Remarkably, when current density is set back to 0.1 C, an excellent capacity retain capability is observed compared to MnO/C, where the capacities are kept between 382 mAh g^{-1} and 398 mAh g^{-1} . The improved electrochemical kinetics is confirmed by electrochemical impedance spectroscopy (EIS) (Figure 9). The R_{ct} value represents the charge transfer impedances. Due to the addition of CNTs, the charge transfer impedances after 3 cycles and 100 cycles are greatly reduced compared to the bare MnO/C. Particularly, after 100 cycles, the resistances of MnO/C/CNTs are reduced by a factor of 5 (Table 1).

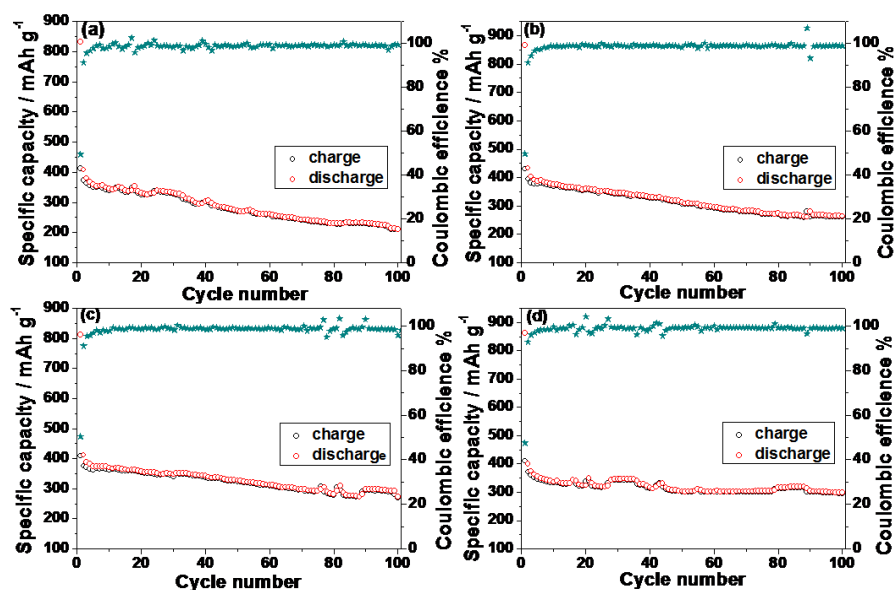


Fig. 7. Cycling performance of MnO/C/CNTs nanohybrids with different contents of carbon nanotubes: (a) 0 %, (b) 2.5 %, (c) 5.0 %, and (d) 10.0 %. Voltage range: 3 V - 0.005 V vs. Li/Li⁺, current density: 0.2 C (151 mA g^{-1}).

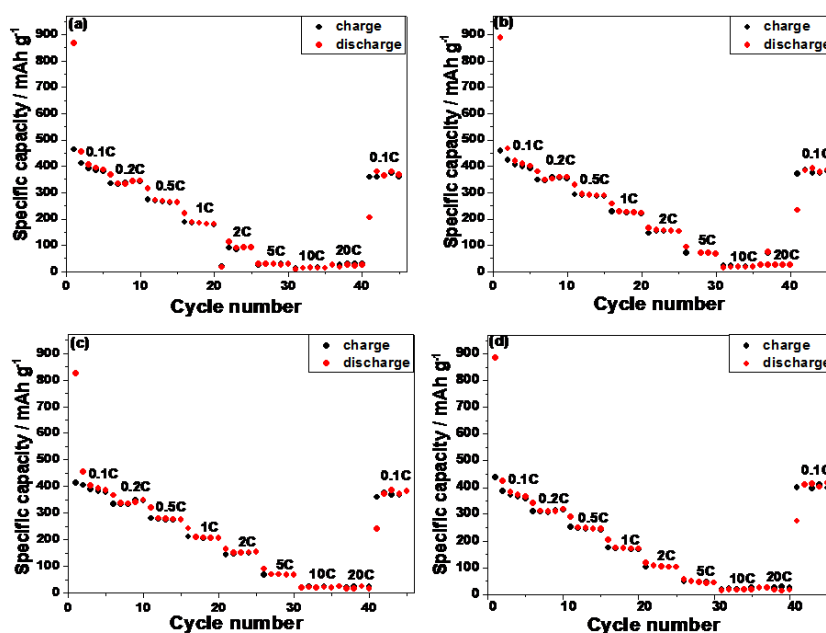


Fig. 8. Rate performance of MnO/C/CNTs nanohybrids with different contents of carbon nanotubes at current density consequence of 0.1 C, 0.2 C, 0.5 C, 1 C, 2C, 5 C, 10 C, 20 C and 0.1 C. (a) 0 %, (b) 2.5 %, (c) 5.0 %, and (d) 10.0 %.

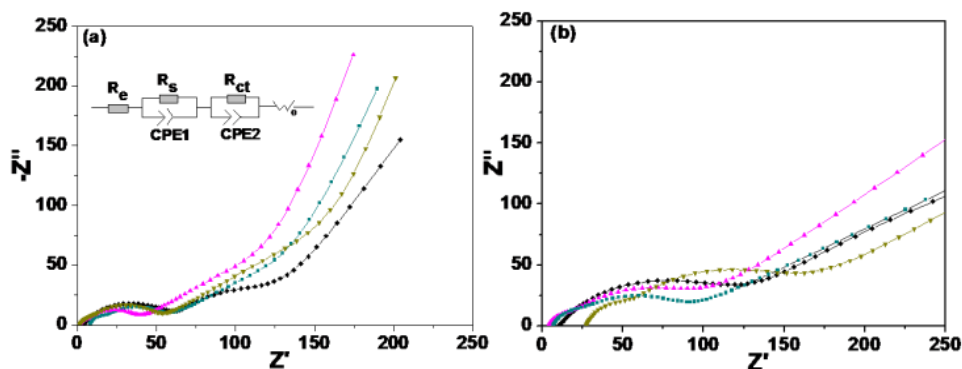


Fig. 9. Electrochemical impedance spectra (EIS) of MnO/C/CNTs with different mass contents of CNTs after 3 cycles (a) and after 100 cycles (b), 0 %: black; 2.5 %: dark yellow; 5.0 %: magenta; 10.0 %: dark cyan.

Table 1. Charge transfer impedance of MnO/C/CNTs electrodes after 3 cycles and 100 cycles at 0.2 C.

	R_{ct} -3cy (Ω)	R_{ct} -100cy (Ω)
0 % CNTs	60.5	449.4
2.5 % CNTs	39.7	86.1
5.0 % CNTs	29.7	69.7
10.0 % CNTs	13.1	56.3

The cyclic voltammetry (CV) test was performed for the initial three cycles at a scanning rate of 0.1 mV s^{-1} with the voltage range between 3.0 V and 0.01 V vs. Li^+/Li at room temperature. As depicted in Figure 10, in the first cathodic process for different contents of CNTs (0 %, 2.5 %, 5.0 %, and 10.0 %, respectively), an irreversible reduction peak at around 0.76 V corresponds to the irreversible decomposition of electrolyte and the formation of a solid electrolyte interphase (SEI) layer [32, 33]. A weak peak at low potential nearly 0.18 V represents the reduction of Mn^{2+} to metallic Mn. A typical oxidation peak at around 1.27 V suggests the conversion reaction which metallic Mn converted to the +2 valence state of Mn.

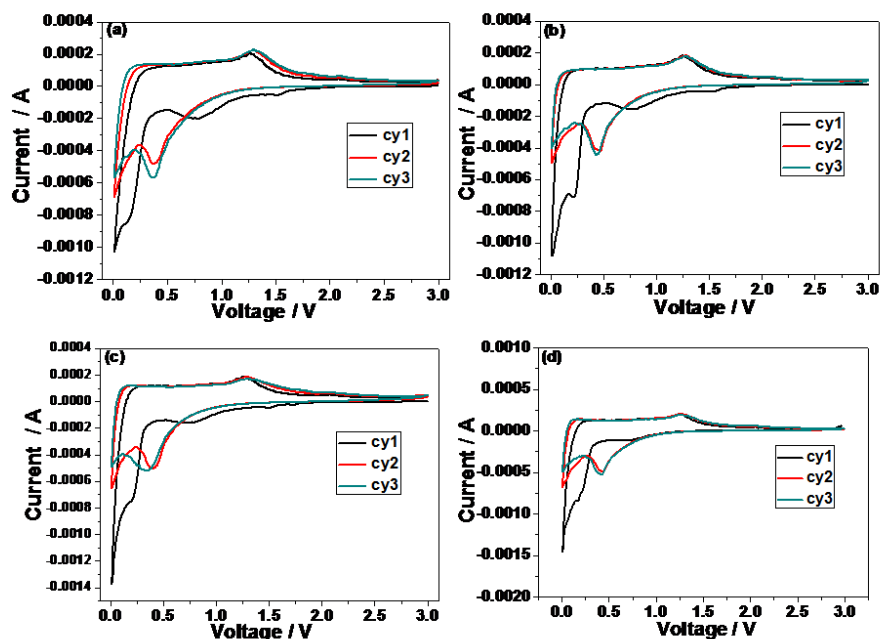


Fig. 10. CV curves of $\text{MnO}/\text{C}/\text{CNTs}$ nanohybrids with different contents of carbon nanotubes: (a) 0 %, (b) 2.5 %, (c) 5.0 %, and (d) 10.0 %. Scan rate: 0.1 mV S^{-1} , in the voltage range of 3 V - 0.01 V vs. Li^+/Li .

4. Conclusions

In this work, $\text{MnO}/\text{C}/\text{CNTs}$ nanohybrids using dental resin monomers as solvent and carbon source have been successfully synthesized. The *in situ* formed Manganese (II) oxide nanoparticles are homogeneously embedded in the *in situ* formed carbon matrix, where CNTs are homogeneously dispersed. Significant improvement on the rate performance has been achieved due to the incorporation of CNTs compared to the bare MnO/C nanohybrid. It is due to the reduction of charge transfer impedance of the nanohybrids as confirmed by the electrochemical impedance spectroscopy. The work addressed in this work provides a new method to synthesize transition metal oxide/carbon nanohybrids for lithium-ion battery anode. It can be extended to other anode system and inspiring for the functional nanocomposite area. Further work on the synthesis of other anode based on this concept is in progress and will be addressed in future publications.

Acknowledgements

This research is funded by the National Natural Science Foundation of China (51103172), the Zhejiang Nonprofit Technology Applied Research Program (2013C33190), the open project of the Beijing National Laboratory for Molecular Science (20140138), and Ningbo Key Laboratory of Polymer Materials. Donation of the dental resins from Esstech, Inc., USA, is greatly appreciated.

Reference

- [1] A. Magasinski, P. Dixon, B. Hertzberg, A. Kvit, J. Ayala, G. Yushin, *Nature Mater.* **9**, 353 (2010).
- [2] H. Li, Z.X. Wang, L.Q. Chen, X.J. Huang, *Adv. Mater.* **21**, 4593 (2009).
- [3] J. Cabana, L. Monconduit, D. Larcher, M.R. Palacin, *Adv. Mater.* **22**, E170 (2010).
- [4] J.Y. Ji, H.X. Ji, L.L. Zhang, X. Zhao, X. Bai, X.B. Fan, F.B. Zhang, R.S. Ruoff, *Adv. Mater.* **25**, 4673 (2013).
- [5] H. Jiang, Y.J. Hu, S.J. Guo, C.Y. Yan, P.S. Lee, C.Z. Li, *ACS Nano* **8**, 6038 (2014).
- [6] P. Poizot, S. Laruelle, S. Grugeon, L. Dupont, J.M. Tarascon, *Nature*. **407**, 496 (2000).
- [7] X. Wang, X.L. Wu, Y.G. Guo, Y.T. Zhong, X.Q. Cao, Y. Ma, J.N. Yao, *Adv. Funct. Mater.* **20**, 1680 (2010).
- [8] B. Xu, C.R. Fell, M.F. Chi, Y.S. Meng, *Energy & Environmental Science*. **4**, 2223 (2011).
- [9] F. Kopnov, R. Tenne, *Dig. J. Nanomater. Biostruct.* **3**,123 (2008).
- [10] C.K. Chan, H.L. Peng, G. Liu, K. McIlwrath, X.F. Zhang, R.A. Huggins, Y. Cui, *Nat. Nanotechnol.* **3**, 31 (2008).
- [11] U. Kasavajjula, C.S. Wang, A.J. Appleby, *J. Power Sources*. **163**, 1003 (2007).
- [12] M.H. Park, M.G. Kim, J. Joo, K. Kim, J. Kim, S. Ahn, Y. Cui, J. Cho, *Nano Lett.* **9**, 3844 (2009).
- [13] G.L. Cui, L. Gu, L.J. Zhi, N. Kaskhedikar, P.A. van Aken, K. Mullen, J. Maier, *Adv. Mater.* **20**, 3079 (2008).
- [14] J. Graetz, C.C. Ahn, R. Yazami, B. Fultz, *J. Electrochem. Soc.* **151**, A698 (2004).
- [15] D.J. Xue, S. Xin, Y. Yan, K.C. Jiang, Y.X. Yin, Y.G. Guo, L.J. Wan, *JACS* **134**, 2512 (2012).
- [16] Y. Idota, T. Kubota, A. Matsufuji, Y. Maekawa, T. Miyasaka, *Science*. **276**, 1395-1397 (1997).
- [17] T. Brousse, R. Retoux, U. Herterich, D.M. Schleich, *J. Electrochem. Soc.* **145**, 1-4 (1998).
- [18] S.J. Han, B.C. Jang, T. Kim, S.M. Oh, T. Hyeon, *Adv. Funct. Mater.* **15**, 1845-1850 (2005).
- [19] B. Sun, Z.X. Chen, H.S. Kim, H. Ahn, G.X. Wang, *J. Power Sources*. **196**, 3346-3349 (2011).
- [20] Y. Xia, Z. Xiao, X. Dou, H. Huang, X.H. Lu, R.J. Yan, Y.P. Gan, W.J. Zhu, J.P. Tu, W.K. Zhang, X.Y. Tao, *ACS Nano* **7**, 7083 (2013).
- [21] X.-H. Ma, Q.-Y. Wan, X. Huang, C.-X. Ding, Y. Jin, Y.-B. Guan, C.-H. Chen, *Electrochim. Acta.* **121**, 15 (2014).
- [22] A. Debart, L. Dupont, P. Poizot, J.B. Leriche, J.M. Tarascon, *J. Electrochem. Soc.* **148**, A1266 (2001).
- [23] X. Fang, X. Lu, X. Guo, Y. Mao, Y.-S. Hu, J. Wang, Z. Wang, F. Wu, H. Liu, L. Chen, *Electrochem. Commun.* **12**, 1520 (2010).

- [24] J. Liu, Q. Pan, *Electrochem. Solid-State Lett.* **13**, A139 (2010).
- [25] S.W. Lee, J. Kim, S. Chen, P.T. Hammond, Y. Shao-Horn, *ACS Nano* **4**, 3889 (2010).
- [26] X.F. Sun, Y.L. Xu, P. Ding, G.G. Chen, X.Y. Zheng, R. Zhang, L. Li, *J. Power Sources*. **255**, 163 (2014).
- [28] Y. Xiao, X. Wang, Y. Xia, Y. Yao, E. Metwalli, Q. Zhang, R. Liu, B. Qiu, M. Rasool, Z. Liu, J.-Q. Meng, L.-D. Sun, C.-H. Yan, P. Muller-Buschbaum, Y.-J. Cheng, *ACS Appl. Mater. Interfaces*. **6**, 18461 (2014).
- [29] X. Wang, J.-Q. Meng, M. Wang, Y. Xiao, R. Liu, Y. Xia, Y. Yao, E. Metwalli, Q. Zhang, B. Qiu, Z. Liu, J. Pan, L.-D. Sun, C.-H. Yan, P. Mueller-Buschbaum, Y.-J. Cheng, *ACS Appl. Mater. Interfaces*. **7**, 24247 (2015).
- [30] Y.H. Dai, H. Jiang, Y.J. Hu, C.Z. Li, *RSC Adv.* **3**, 19778 (2013).
- [29] C.X. Yang, Q.M. Gao, W.Q. Tian, Y.L. Tan, T. Zhang, K. Yang, L.H. Zhu, *J. Mater. Chem A* **2**, 19975 (2014).
- [31] X.N. Li, Y.C. Zhu, X. Zhang, J.W. Liang, Y.T. Qian, *RSC Adv.* **3**, 10001 (2013).
- [32] J. Jiang, Y. Li, J. Liu, X. Huang, C. Yuan, X.W. Lou, *Adv. Mater.* **24**, 5166 (2012).
- [33] M.S. Wu, P.C.J. Chiang, J.T. Lee, J.C. Lin, *J. Phys. Chem. B* **109**, 23279 (2005).